

O2O-Afford: Annotation-Free Large-Scale Object-Object Affordance Learning

Kaichun Mo¹, Yuzhe Qin², Fanbo Xiang², Hao Su², Leonidas Guibas¹

¹Stanford University ²UCSD

<https://cs.stanford.edu/~kaichun/o2oafford>

Abstract: Contrary to the vast literature in modeling, perceiving, and understanding agent-object (*e.g.* human-object, hand-object, robot-object) interaction in computer vision and robotics, very few past works have studied the task of object-object interaction, which also plays an important role in robotic manipulation and planning tasks. There is a rich space of object-object interaction scenarios in our daily life, such as placing an object on a messy tabletop, fitting an object inside a drawer, pushing an object using a tool, etc. In this paper, we propose a unified affordance learning framework to learn object-object interaction for various tasks. By constructing four object-object interaction task environments using physical simulation (SAPIEN) and thousands of ShapeNet models with rich geometric diversity, we are able to conduct large-scale object-object affordance learning without the need for human annotations or demonstrations. At the core of technical contribution, we propose an object-kernel point convolution network to reason about detailed interaction between two objects. Experiments on large-scale synthetic data and real-world data prove the effectiveness of the proposed approach.

Keywords: Object-object Affordance, Vision for Robotics, Large-scale Learning

1 Introduction

We humans accomplish everyday tasks by interacting with a wide range of objects. Besides mastering the skills of manipulating objects using our fingers (*e.g.* grasping [1]), we must also understand the rich space of object-object interactions. For instance, to put a book inside a bookshelf, not only do we need to pick up the book by our hand, to place it, we still have to figure out possible good slots — the distance between the two shelf boards must be larger than the book height, and the slot should afford the book at a suitable pose. For us humans, we can instantly form such understanding of object-object interactions after a glance of the scene. Theories in cognitive science [2] conjecture that this is because human beings have learned certain priors for object-object interactions based on the shape and functionality of objects. Can intelligent robot agents acquire similar priors and skills?

While there is a plethora of literature studying agent-object interaction, very few works have studied the important task of object-object interaction. In an earlier work, Sun *et al.* [3] proposed to use Bayesian network to model human-object-object interaction and performed experiments on a small-scale (six objects in total) labeled training data with relative motions of humans and the two objects. Another relevant work by Zhu *et al.* [4] studied the problem of tool manipulation, which is an important special case of object-object interaction, and proposed a learning framework given RGB-D scanned human and object demonstration sequences as supervision signals. Both works modeled object-object interaction in a small scale and trained the models with human annotations or demonstrations. In contrary, we propose a large-scale solution by learning from simulated interactions without any need for human annotations or demonstrations.

In this paper, we consider the problem of learning object-object interaction priors (abbreviated as the *O2O priors* for brevity). Particularly, in our setup, we consider an acting object that is directly manipulated by robot actuators, and a 3D scene that will be interacted upon. We are interested in encoding and predicting the set of feasible geometric relationships when the acting object is afforded by objects in the scene along accomplishing a certain specified task. One important usage of our

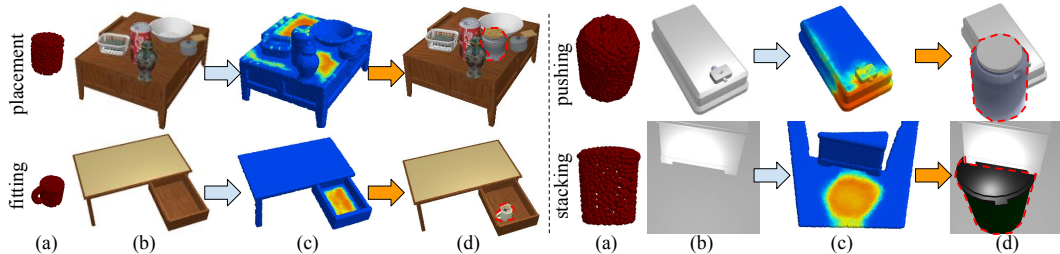


Figure 1: **The O2O-Afford Framework and Tasks.** For a given object-object interaction task (*i.e.* placement, fitting, pushing, stacking), our method takes as inputs a 3D acting object point cloud (a) and a partial 3D scan of the scene/object (b), and outputs an affordance prediction heatmap (c) that estimates the likelihood of the acting object successfully accomplishing the task at every pixel. At the test time, one may easily sample a position from the heatmap to perform the action (d).

O2O priors is to reduce the search space for downstream planning tasks. For example, to place a big object inside a cabinet having a few drawers with various sizes, the *O2O priors* may rule out those small drawers without any interaction trials and identify the ones big enough for the motion planners. Then, for the identified drawers, the *O2O priors* may further propose where the acting object could be placed by considering other factors, such as collision avoidance with existing objects in the drawers.

Next, we introduce how we encode the *O2O priors*. We formulate a per-point affordance labeling framework (Fig. 1) that unifies representations for various kinds of object-object interaction tasks. Given as input the acting object in different geometry, orientations and sizes, along with a partial 3D scan of an existing scene, we produce a point-wise affordance heatmap on the scene that measures the likelihood for each point on the scene point cloud of successfully accomplishing the task.

The affordance labels for supervision are generated by simulating the object-scene interaction process. Using the SAPIEN physical simulator [5] and large-scale 3D shape datasets [6, 7], we build up a large-scale learning-from-interaction benchmark that covers a rich space of object-object interaction scenarios. Fig. 1 illustrates the four diverse tasks we use in this work, in which different visual, geometric and dynamic attributes are essential to be learned for accurately modeling the task semantics. For example, to place a jar on a messy table, one need to find a flat tabletop area with enough space considering the volume of the jar; to fit a mug inside a drawer, the size and height of the drawer has to be big enough to contain the mug; etc.

As a core technical contribution, we propose an object-kernel point convolution network to reason about detailed geometric constraints between the acting object and the scene. We perform large-scale training and evaluation over 1,785 shapes from 18 object categories. Experiments prove that our proposed method learns effective features reasoning about the contact geometric details and task semantics, and show promising results not only on novel shapes from the training categories, but also over unseen object categories and real-world data.

In summary, our contributions are:

- we revisit the important problem of object-object interaction and propose a large-scale annotation-free learning-from-interaction solution;
- we propose a per-point affordance labeling framework, with an object-kernel point convolution network, to deal with various object-object interaction tasks;
- we build up four benchmarking environments with unified specifications using SAPIEN [5] and ShapeNet [6, 7] that covers various kinds of object-object interaction tasks;
- we show that the learned visual priors provide meaningful semantics and generalize well to novel shapes, unseen object categories, and real-world data.

2 Related Works

Learning from Interaction. Annotating training data has always been a heavy burden for supervised learning tasks. In robotics community, there has been growing interest in scaling up data collection via self-supervised interaction. This approach has been widely used to learn robot manipulation skills [8, 9, 10, 11], facilitate object representation learning [12, 13, 14], and improve the result of perception tasks, *e.g.* segmentation [15, 16], pose estimation [17]. However, collecting interaction

experience by a real robot is slow and even unsafe. A surrogate solution is physical simulation. Recent works explore the possibility of using data collected from simulation to train perception model [18, 19, 20]. By leveraging the interactive nature of physical simulation, researchers can also train network to reason object dynamics, *e.g.* mass [21], force [22], stability [23]. Benefits from the large-scale ShapeNet [6, 7] models, we can collect various type of interaction data from simulators.

Agent-Object Interaction Affordance. Agent-object interaction affordance describes how agents may interact with objects. The most common kind is grasping affordance. Recent works [24, 25, 26, 27, 28] formulate grasping as visual affordance detection problems that anticipate the success of a given grasp. An affordance detector predicts the graspable area from image or point cloud for robot grippers. Other works [29, 30, 31, 32] extend contact affordance from simple robot gripper to more complex human object interaction. However, most of the works require additional annotation as training data [24, 25, 29]. Recently, it was shown that visual affordances can also be reasoned from human demonstration videos in a weakly-supervised manner [33, 34]. Recent works [35, 36, 37] proposed automated methods for large-scale agent-object visual affordance learning.

Object-Object Interaction Affordance. Very few works have explored learning object-object interaction affordance. Sun *et al.* [3] built an object-object relationship model and associated it with a human action mode. It shows that the learned affordance is beneficial for downstream robotic manipulation tasks. Another line of works on object-object affordance focus on one particular object relationship: tool manipulation [4], object placement [38], pouring [39], and cooking [40]. However, all these works are performed on a limit number of objects. Most of these works also require human annotations or demonstrations. In our work, we conduct large-scale annotation-free affordance learning that covers various kinds of object-object interaction with diverse shapes and categories.

3 Problem Formulation

For every object-object interaction task, there are two 3D point cloud inputs: a scene partial scan $S \in \mathbb{R}^{n \times 3}$, and a complete acting object point cloud $O \in \mathbb{R}^{m \times 3}$, with center $c \in \mathbb{R}^3$, 1-DoF orientation $q \in [0, 2\pi)$ along the up-direction and an isotropic scale $\alpha \in \mathbb{R}$. The two point clouds are captured by the same camera and are both presented in the camera base coordinate frame, with the z -axis aligned with the up direction and the x -axis points to the forward direction. The output of our O2O-Affordance tasks is a point-wise affordance heatmap $A \in [0, 1]^m$ for every point in the scene point cloud, indicating the likelihood of the acting object successfully interacting with the scene at every position. Fig. 1 shows example inputs and outputs for four different tasks.

4 Task Definition and Data Generation

As summarized in Fig. 1, we consider four object-object interaction tasks: placement, fitting, pushing, stacking. While *placement* and *stacking* are commonly used in manipulation benchmark [41, 42, 43, 44], the *fitting* and *pushing* tasks are also interesting for bin packing [45] and tool manipulation applications [46]. One may create more task environments depending on downstream applications. Although having different task semantics and requiring learning of distinctive geometric, semantic, or dynamic attributes, we are able to unify the task specifications to share the same framework.

4.1 Unified Task Environment Framework

Task Initialization and Inputs. Each task starts with creating a static scene, including one or many randomly selected ShapeNet models and a possible ground floor. Some objects in the scene may have articulated parts with certain starting part poses, depending on different tasks. The scene objects may be fixed to be always static (*e.g.* when we assume a cabinet is very heavy), or dynamic but of zero velocity at the beginning of the simulation (*e.g.* for an object on the ground to be pushed). In all cases, a camera takes a single snapshot of the scene to obtain a scene partial 3D scan S as the input to the problem. Fig. 2 (a) illustrate example initialization scenarios in the four task environments. To interact with the scene, we then randomly fetch an acting object and initialize it with random orientation and size. We provide a complete 3D point cloud O , in the same camera coordinate frame as the scene point cloud, as another input to the problem.

O2O Priors Parametrization. For each task \mathcal{T} , we define the *O2O priors* of an acting object O interacting with a scene geometry S as a per-point affordance heatmap $A_{\mathcal{T}} \in [0, 1]^m$ over the scene point cloud $S \in \mathbb{R}^{m \times 3}$. For each point $p_i \in S$, we predict a likelihood $a_i \in [0, 1]$ of the acting object O

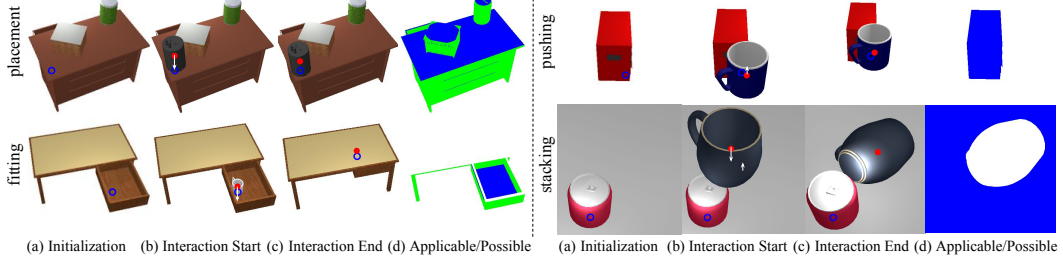


Figure 2: **Task Environment Specifications and Trajectory Illustrations.** For each task environment, from left to right, we respectively show the static scene for initialization (a), the state of objects at the beginning of interaction (b), the state of objects at the end of interaction (c), as well as the applicable (green+blue) and possible (blue) regions (d). We mark the interacting positions p in blue circles and track the moving object centers c using red dots. The white arrows used in (b) indicate the object trajectory moving directions: forward direction for *pushing*; gravity direction for others.

successfully interacting with the scene S at position p_i following a parametrized short-term trajectory $\tau_{\bar{x}}(p_i)$, which is a hard-coded task-specific trajectory with the acting object center initialized at $c_i = p_i + r_{\bar{x}}(O)$. Here, $r_{\bar{x}}(O) \in \mathbb{R}^3$ is a task-specific offset that also depends on the acting object O . Fig. 2 (b) illustrates the starting states of the acting and scene objects, where red dots track the object centers c_i 's and blue circles mark the interacting position p_i 's, from which one may imagine the offsets $r_i = c_i - p_i$ for different tasks. We will define the task-specific offsets in Sec. 4.2.

Simulated Interaction Trajectory. For each interaction trial, we execute a hard-coded short-term trajectory $\tau_{\bar{x}}(p_i)$ to simulate the interaction between the acting object O and the scene objects S at position p_i . Every motion trajectory is very short, *e.g.* taking place within < 0.1 unit length, so that it can be preceded by long-term task trajectories, to make the learned visual priors possibly useful for many downstream tasks. The white arrows in Fig. 2 (b) show the trajectory moving directions – the forward direction for *pushing* and the gravity direction for the other three environments. The executed hard-coded trajectories are always along straight lines, though the final object state trajectories may be of free forms due to the object collisions. Fig. 2 (c) present some example ending object states.

Applicable and Possible Regions. For every simulated interaction trial, we randomly pick p over the regions where the task is applicable and possible to succeed. Some scene points may not be applicable for a specific task. For example, for the *stacking* task, only points on the ground are applicable since we have to put the acting object on the floor for the scene object to stack over. Among applicable points, we only try the positions that are possible to be successfully interacted and directly mark the impossible points as failed interactions. For example, impossible points include the positions whose normal directions are not nearly facing upwards for the *placement* and *fitting* tasks. Fig. 2 (d) illustrate example applicable and possible masks over the input scene geometry.

Metrics and Outcomes. For each interaction trial, the outcome could be either successful or failed, measured by task-specific metrics. The metric measures if the intended task semantics has been accomplished, by detecting state changes of the acting and scene objects during the interaction and at the end. For example, in Fig. 2 (c), the *fitting* example shows that the drawer will be driven to close to check if the acting object can be fitted inside the drawer. See Sec. 4.2 for detailed definitions.

4.2 Four Task Environments

Placement. Each scene is initialized with a static root object (*e.g.* a table) with 0~15 movable small item objects randomly placed on the root object to simulate a messy tabletop. The root object may have articulated parts, which are initialized to be closed or of a random starting pose with equal probabilities. The acting object is another small item object to be placed. All points are applicable on the scene, but only the positions with normal directions that are close enough to the world up-direction are possible. For the acting object center at start, we have an up-directional offset $r_z = s_z/2 + 0.01$, where s_z is the up-directional object size, so that the acting object is 0.01 unit length away from contacting the intended interaction position p . The motion trajectory is along the gravity direction. The metric for success is: 1) the acting object has no collision at start; 2) the acting object finally stays on the countertop; and 3) the acting object drops off stably with no big orientation change.

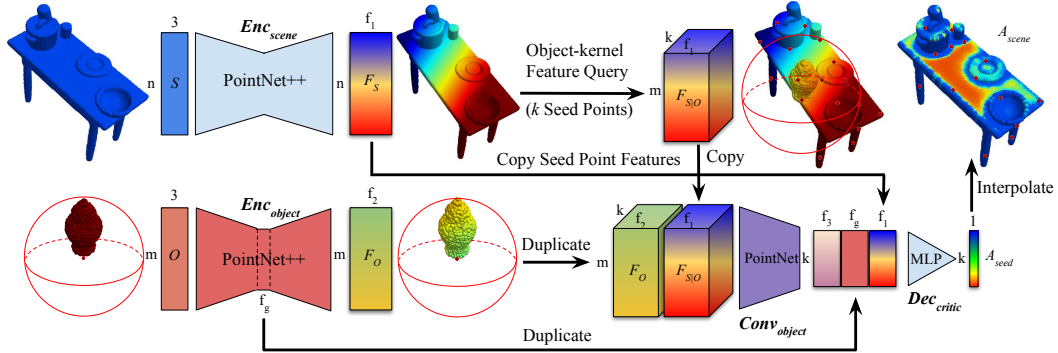


Figure 3: **Network Architecture.** Taking as inputs a partial 3D scan of the scene S (dark blue) and a complete 3D point cloud of acting object O (dark red), our network learns to extract per-point features on both inputs, correlate the two point cloud feature maps using an object-kernel point convolution, and finally predict a point-wise affordance heatmap over the scene point cloud.

Fitting. The scene contains only one static root object with articulated parts (*e.g.*, doors, drawers). At least one articulated part is randomly opened, while the other parts may be closed or randomly opened with equal probabilities. The acting object is a small item object to be fitted inside the drawer or shelf board. All points except the countertop points are applicable, since placing the item on countertop is concerned by the *placement* task. The positions with normal directions close enough to the world up-direction are possible. The starting acting object center and the motion trajectory are the same as in the *placement* task. Besides the three criteria for *placement*, there is one additional checking point for the metric: the door or drawer can be closed containing the acting object without being blocked.

Pushing. The scene object is dynamically placed on an invisible ground, initialized with zero velocity, and guaranteed to be stable by itself. There is no part articulation allowed in this task. The acting object is a small item object to push the scene object. All points on the scene are applicable and possible. The starting acting object center has offsets $r_x = -s_x/2 - 0.1$, $r_z = s_z/2 + 0.02$ where s_x and s_z are respectively the forward-directional and up-directional object sizes. The acting object moves along the forward-direction to push the scene object. The metric for success is: 1) the acting object has no collision at start; 2) there is a big enough motion of the scene object; 3) the actual moving direction is within 30° aligned with the forward-direction; and 4) the scene object does not topple.

Stacking. We first place a dynamic acting object stably with zero velocity on a visible ground. Then, we pick a second item as the scene object to stack over the acting object. We simulate the stacking interaction that drops the scene object on top of the acting object. For the cases that the two objects finally touch each other and stay stably on the ground, we consider a stacking task based on the final two object states. The scene object is initialized at the final stably stacking pose. All points on the ground are applicable and possible. The acting object center has an up-directional offset $r_z = s_z/2$, where s_z is the up-directional object size. The metric for success is that the acting object has no big pose (center+orientation) change before and after the stacking interaction.

5 Method for Affordance Prediction

We propose a unified 3D point-based method, with an object-kernel point convolution network, to tackle the various O2O-Afford tasks. Though very simple, this method is quite effective and efficient in reasoning about the detailed geometric contacts and constraints.

5.1 Network Architecture

Fig. 3 illustrates the proposed pipeline. We describe each network module in details below.

Feature Extraction Backbones. We employ two segmentation-version PointNet++ [47] to extract per-point feature maps for the two input point clouds. We first normalize them to be zero-centered. For the 3D partial scene $S \in \mathbb{R}^{n \times 3}$, we train a $\mathbf{Enc}_{\text{scene}}$ PointNet++ to extract per-point feature map $F_S \in \mathbb{R}^{n \times f_1}$. For the 3D acting object $O \in \mathbb{R}^{m \times 3}$, we use another $\mathbf{Enc}_{\text{object}}$ PointNet++ to obtain per-point feature map $F_O \in \mathbb{R}^{m \times f_2}$ and a global feature for the acting object $F_g \in \mathbb{R}^{f_g}$.

Object-kernel Point Convolution. Our O2O-Afford tasks require reasoning about the contact geometric constraints between the two input point clouds. Thus, we design an object-kernel

convolution module that uses the acting object as an explicit object kernel to slide over a subsampled scene seed points and performs point convolution operation to aggregate per-point features between the acting object and the scene inputs. This design shares a similar spirit to the recently proposed Transporter networks [48], but we carefully curate it for the 3D point cloud convolution setting. One may think of a naive alternative of simply concatenating two point clouds together at every seed point and training a classifier. However, this is computationally too expensive due to several forwarding passes over the two input points clouds with the acting object positioned at different seed locations.

Concretely, on the scene partial point cloud input $S \in \mathbb{R}^{n \times 3}$, we first sample k seed points $\{p_1, p_2, \dots, p_k\} \subset S$ using Furthest Point Sampling (FPS). Then, we move the acting object point cloud $O \in \mathbb{R}^{m \times 3}$, as an explicit query kernel, over each of the sampled seed point p_i to query a scene feature map $F_{S|O, p_i} \in \mathbb{R}^{m \times f_1}$ over the acting object points O . In more details, for each point $o_j \in O$, we query the scene feature at the position $o_j^i = o_j + p_i$ using the inverse distance weighted interpolation [47] in the scene point cloud $S \in \mathbb{R}^{n \times 3}$ with feature map $F_S \in \mathbb{R}^{n \times f_1}$. We query t nearest neighbor points $\{e_1, e_2, \dots, e_t\} \subset S$ to any o (i, j omitted for simplicity), and compute $F_{S|o}$ with

$$F_{S|o} = \frac{\sum_{l=1}^t w_l F_{S|e_l}}{\sum_{l=1}^t w_l}, w_l = \frac{1}{\|o - e_l\|_2}, l = 1, 2, \dots, t, \quad (1)$$

where $F_{S|e_l} \in \mathbb{R}^{f_1}$ is the computed scene feature at point e_l . We aggregate all interpolated scene features $\{F_{S|o_j^i} \in \mathbb{R}^{f_1}\}_j$ over the acting object points $\{o_j^i\}_{j=1,2,\dots,m}$ to obtain a final feature map $F_{S|O, p_i} \in \mathbb{R}^{m \times f_1}$ at every scene seed point p_i .

Concatenating the acting object feature map $F_O \in \mathbb{R}^{m \times f_2}$ and the interpolated scene feature map $F_{S|O, p_i} \in \mathbb{R}^{m \times f_1}$, we obtain an aggregated feature map $F_{SO|O, p_i} \in \mathbb{R}^{m \times (f_1 + f_2)}$ at every scene seed point p_i . We then implement the object-kernel point convolution **Conv_{object}** using PointNet [49] to obtain seed point features $F_{SO|p_i} \in \mathbb{R}^{f_3}$. The PointNet is composed of a per-point Multilayer Perceptron (MLP) transforming every individual point feature and a final max-pooling over all m points.

Point-wise Affordance Predictions. For each scene seed point p_i , we aggregate the information of the computed object-kernel point convolution feature $F_{SO|p_i} \in \mathbb{R}^{f_3}$, the local scene point feature $F_{S|p_i} \in \mathbb{R}^{f_1}$, and the global acting object feature $F_g \in \mathbb{R}^{f_g}$, and feed them through **Dec_{critic}**, implemented as an MLP followed by a Sigmoid activation function, to obtain an affordance labeling $a_{p_i} \in [0, 1]$, with bigger value indicates higher likelihood of a successful interaction between the acting object and the scene at p_i . After computing the per-point affordance labeling for the k subsampled seed points, we interpolate back to all the locations in the scene point cloud, using the inverse distance weighted average, to obtain a final per-point affordance labeling $A_{scene} \in [0, 1]^n$.

5.2 Training and Loss

The whole pipeline is trained in an end-to-end fashion, supervised by the simulated interaction trials with successful or failed outcomes. The scene and acting objects are selected randomly from the training data of the training object categories. We equally sample data from different object categories to address the data imbalance issue. We empirically find that having enough positive data samples (at least 20,000 for task) are essential for a successful training. We train individual networks for different tasks and use the standard binary cross entropy loss. We use $n = 10000$, $m = 1000$, $k = 1000$, $t = 3$, and $f_1 = f_2 = f_3 = f_g = 128$ in the experiments. See supplementary for more training details.

6 Experiments

We use the SAPIEN physical simulator [5], equipped with ShapeNet [6] and PartNet [7] models, to do the experiments. We evaluate our proposed pipeline and provide quantitative comparisons to three baselines. Experiments show that we successfully learned visual priors of object-object interaction affordance for various O2O-Afford tasks, and the learned representations generalize well to novel shapes, unseen object categories, and real-world data.

6.1 Data and Settings

Our experiments use 1,785 ShapeNet [6] models in total, covering 18 commonly seen indoor object categories. We randomly split the different object categories into 12 training ones and 6 test ones. Furthermore, the shapes in the training categories are separated into training and test shapes. In total,

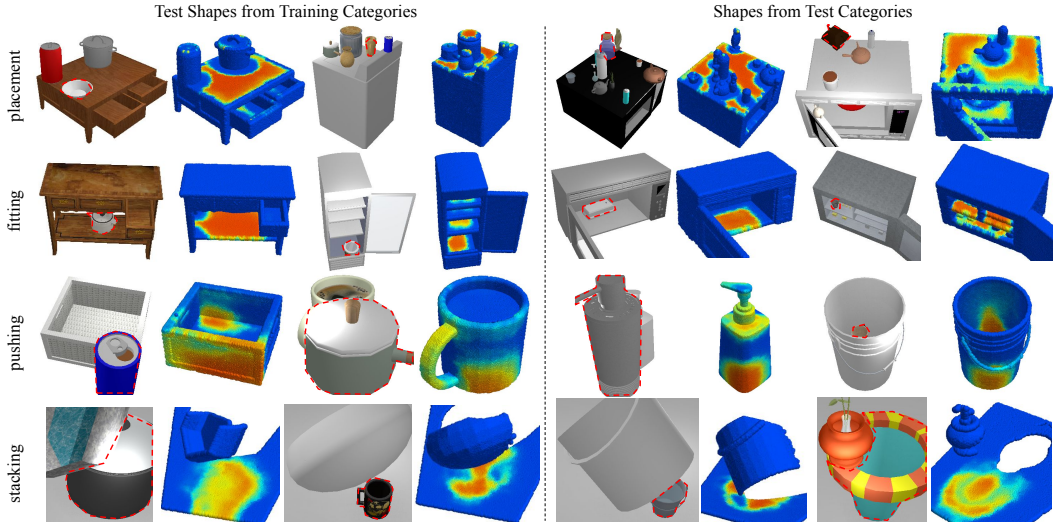


Figure 4: **Qualitative Results.** For each of the tasks, we show examples of our network predictions. Left two examples show test shapes from the training categories, while two right ones are shapes from the test categories. In each pair of result figures, we draw the scene geometry together with the acting object (marked with red dashed boundary) on the left, and show our predicted per-point affordance heatmaps on the right.

		F-score (%)		AP (%)				F-score (%)		AP (%)	
placement	B-PosNor	62.1	81.7	60.5	78.2	pushing	B-PosNor	31.9	34.9	37.0	35.5
	B-Bbox	80.9	90.6	90.5	94.5		B-Bbox	33.2	35.0	39.2	37.6
	B-3Branch	63.8	77.1	69.8	82.3		B-3Branch	35.2	36.6	42.2	36.4
	Ours	81.4	90.0	91.1	95.2		Ours	35.5	40.3	46.9	43.1
fitting	B-PosNor	45.4	59.3	46.8	66.7	stacking	B-PosNor	79.3	77.9	79.9	76.5
	B-Bbox	69.5	79.5	80.1	80.6		B-Bbox	85.7	83.2	87.7	87.2
	B-3Branch	48.2	56.9	47.1	60.7		B-3Branch	87.3	84.8	90.8	88.2
	Ours	73.6	80.3	80.1	86.3		Ours	89.6	87.5	91.7	90.8

Table 1: **Quantitative Evaluations.** We compare to three baselines **B-PosNor**, **B-Bbox**, and **B-3Branch**. In each entry, we report evaluations over test shapes from the training categories (before slash) and shapes in the test categories (after slash). Higher numbers indicate better performance.

there are 867 training shapes from the training categories, 281 test shapes from the training categories, and 637 shapes from the test categories. During training, all the networks are trained on the same split of training shapes from the training categories. We then evaluate and compare the methods by evaluating on the test shapes from the training categories, to test the performance on novel shapes from known categories, and the shapes in the test categories, to measure how well the learned visual representations generalize to totally unseen object categories. See supplementary for more details.

6.2 Baselines and Metric

We compare to three baseline methods **B-PosNor**, **B-Bbox**, and **B-3Branch**. **B-PosNor** replaces the per-point scene feature with 3-dim position and 3-dim ground-truth normal, while **B-Bbox** uses a 6-dim axis-aligned bounding box extents to replace the acting object geometry input. We compare to these two baselines to validate that the extracted scene features contain more information than simple normal directions and that object geometry matters. **B-3Branch** implements a naive baseline that employs two PointNet++ branches to process the acting object and scene point clouds as well as an additional branch taking as input the seed point position. Comparison to this baseline can help illustrate the necessity of correlating the two input point clouds. We use a success threshold 0.5 and employ two commonly used metrics: *F-score* and *Average-Precision (AP)*.

6.3 Results and Analysis

Table 1 shows the quantitative evaluations and comparisons. It is clear to see that our method performs better than the three baselines in most entries. We visualize our network predictions in Fig. 4, where we observe meaningful per-point affordance labeling heatmaps on both test shapes from the training categories and shapes in unseen test categories. For *placement*, the network learns to not only find

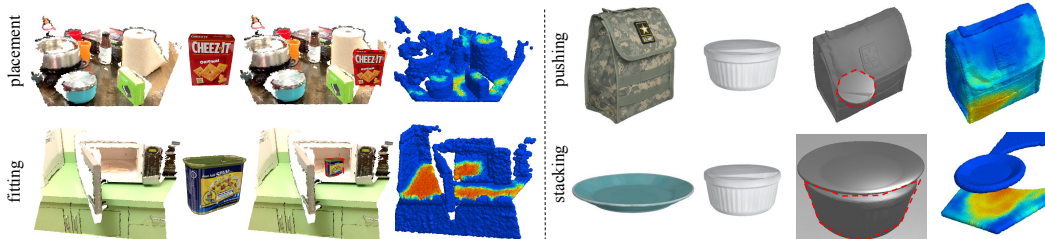


Figure 5: **Results on Real-world Data.** From left to right: we respectively show the scene geometry (a partial 3D scan from the camera viewpoint), the acting object (a complete 3D point cloud), the interaction snapshot (to illustrate the poses and sizes of the objects), and our point-wise affordance predictions. We scan noisy 3D partial scenes using an iPad Pro and choose acting objects from the YCB Dataset [50] in the *placement* and *fitting* examples, while evaluating over three Google Scanned Objects [51, 52, 53] in the rest. In the *fitting* case, only the predictions within the microwave are desired since the network is trained and expected to be tested over clean single scene objects.

		F-score (%)	AP (%)
placement	Ablated	82.2 / 91.3	90.0 / 95.3
	Ours	81.4 / 90.0	91.1 / 95.2
fitting	Ablated	68.0 / 78.3	77.8 / 84.2
	Ours	73.6 / 80.3	80.1 / 86.3
pushing	Ablated	34.9 / 38.6	40.5 / 39.5
	Ours	35.5 / 40.3	46.9 / 43.1
stacking	Ablated	82.6 / 80.4	87.2 / 83.5
	Ours	89.6 / 87.5	91.7 / 90.8

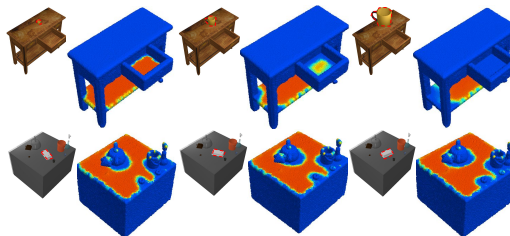


Table 2: **Ablation Study.** We compare to an ablated version that removes the computed object-kernel point convolution features $F_{SO|p_i}$.

Figure 6: **Result Analysis.** Our network predictions are sensitive to the acting object size (top-row) and orientation (bottom-row) changes.

the flat surface, but also avoid collisions from the existing objects. We observe similar patterns for *fitting*, with one additional learned constraint to find two shelves with enough height. For *pushing*, one should push an object in the middle to cause big enough motions and at the bottom to avoid toppling. For *stacking*, our network successfully learns where to place the acting object on the ground for the scene object to stack over. See supplementary for more results.

We also perform an ablation study in Table 2 to prove the effectiveness of the proposed object-kernel point convolution. We further illustrate in Fig. 6 that our network predictions are sensitive to the acting object size and orientation changes. In the top-row *fitting* example, increasing the size of the mug reduces the chance of putting it inside the drawer, as the drawer cannot be further closed containing a big mug. For the bottom-row *placement* example, we observe some detailed affordance heatmap changes while we rotate the cuboid-shaped acting object.

We directly try to apply our network trained on synthetic data to real-world 3D scans. Fig. 5 and Fig. F.9 in the supplementary shows some qualitative results. We observe that, though trained on synthetic data only, our network transfers to real-world collected data to reasonable degrees.

7 Conclusion

We revisited the important but underexplored problem of visual affordance learning for object-object interaction. Using state-of-the-art physical simulation and the available large-scale 3D shape datasets, we proposed a learning-from-interaction framework that automates object-object interaction affordance learning without the need of having any human annotations or demonstrations. Experiments show that we successfully learned visual affordance priors that generalize well to novel shapes, unseen object categories, and real-world data.

Limitations and Future Works. First, our method assumes uniform density for all the objects. Future works may annotate such physical attributes for more accurate results. Second, we train separate networks for different tasks. Future study could think of a way for joint training, as many features may be shared across tasks. Third, there are many more kinds of object-object interaction that we have not included in this paper. People may extend the framework to cope with more tasks.

Acknowledgements

This research was supported by NSF grant IIS-1763268, NSF grant RI-1763268, a grant from the Toyota Research Institute University 2.0 program¹, a Vannevar Bush faculty fellowship, and gift money from Qualcomm. This work was also supported by AWS Machine Learning Awards Program.

References

- [1] A. Saxena, J. Driemeyer, and A. Y. Ng. Robotic grasping of novel objects using vision. *The International Journal of Robotics Research*, 27(2):157–173, 2008.
- [2] R. E. O’Donnell, A. Clement, and J. R. Brockmole. Semantic and functional relationships among objects increase the capacity of visual working memory. *Journal of Experimental Psychology: Learning, Memory, and Cognition*, 44(7):1151, 2018.
- [3] Y. Sun, S. Ren, and Y. Lin. Object–object interaction affordance learning. *Robotics and Autonomous Systems*, 62(4):487–496, 2014.
- [4] Y. Zhu, Y. Zhao, and S. Chun Zhu. Understanding tools: Task-oriented object modeling, learning and recognition. In *Proceedings of the IEEE Conference on Computer Vision and Pattern Recognition*, pages 2855–2864, 2015.
- [5] F. Xiang, Y. Qin, K. Mo, Y. Xia, H. Zhu, F. Liu, M. Liu, H. Jiang, Y. Yuan, H. Wang, et al. Sapien: A simulated part-based interactive environment. In *Proceedings of the IEEE/CVF Conference on Computer Vision and Pattern Recognition*, pages 11097–11107, 2020.
- [6] A. X. Chang, T. Funkhouser, L. Guibas, P. Hanrahan, Q. Huang, Z. Li, S. Savarese, M. Savva, S. Song, H. Su, et al. Shapenet: An information-rich 3d model repository. *arXiv preprint arXiv:1512.03012*, 2015.
- [7] K. Mo, S. Zhu, A. X. Chang, L. Yi, S. Tripathi, L. J. Guibas, and H. Su. Partnet: A large-scale benchmark for fine-grained and hierarchical part-level 3d object understanding. In *Proceedings of the IEEE Conference on Computer Vision and Pattern Recognition*, pages 909–918, 2019.
- [8] L. Pinto and A. Gupta. Supersizing self-supervision: Learning to grasp from 50k tries and 700 robot hours. In *2016 IEEE international conference on robotics and automation (ICRA)*, pages 3406–3413. IEEE, 2016.
- [9] S. Levine, P. Pastor, A. Krizhevsky, J. Ibarz, and D. Quillen. Learning hand-eye coordination for robotic grasping with deep learning and large-scale data collection. *The International Journal of Robotics Research*, 37(4-5):421–436, 2018.
- [10] P. Agrawal, A. Nair, P. Abbeel, J. Malik, and S. Levine. Learning to poke by poking: Experiential learning of intuitive physics. *arXiv preprint arXiv:1606.07419*, 2016.
- [11] L. Pinto, D. Gandhi, Y. Han, Y.-L. Park, and A. Gupta. The curious robot: Learning visual representations via physical interactions. In *European Conference on Computer Vision*, pages 3–18. Springer, 2016.
- [12] Z. Xu, J. Wu, A. Zeng, J. B. Tenenbaum, and S. Song. Densephysnet: Learning dense physical object representations via multi-step dynamic interactions. *arXiv preprint arXiv:1906.03853*, 2019.
- [13] K. Zakka, A. Zeng, J. Lee, and S. Song. Form2fit: Learning shape priors for generalizable assembly from disassembly. In *2020 IEEE International Conference on Robotics and Automation (ICRA)*, pages 9404–9410. IEEE, 2020.
- [14] L. Yen-Chen, A. Zeng, S. Song, P. Isola, and T.-Y. Lin. Learning to see before learning to act: Visual pre-training for manipulation. In *2020 IEEE International Conference on Robotics and Automation (ICRA)*, pages 7286–7293. IEEE, 2020.

¹Toyota Research Institute (“TRI”) provided funds to assist the authors with their research but this article solely reflects the opinions and conclusions of its authors and not TRI or any other Toyota entity.

- [15] D. Pathak, Y. Shentu, D. Chen, P. Agrawal, T. Darrell, S. Levine, and J. Malik. Learning instance segmentation by interaction. In *Proceedings of the IEEE Conference on Computer Vision and Pattern Recognition Workshops*, pages 2042–2045, 2018.
- [16] A. Eitel, N. Hauff, and W. Burgard. Self-supervised transfer learning for instance segmentation through physical interaction. In *2019 IEEE/RSJ International Conference on Intelligent Robots and Systems (IROS)*, pages 4020–4026. IEEE, 2019.
- [17] X. Deng, Y. Xiang, A. Mousavian, C. Eppner, T. Bretl, and D. Fox. Self-supervised 6d object pose estimation for robot manipulation. In *2020 IEEE International Conference on Robotics and Automation (ICRA)*, pages 3665–3671. IEEE, 2020.
- [18] Z. Fang, A. Jain, G. Sarch, A. W. Harley, and K. Fragkiadaki. Move to see better: Towards self-supervised amodal object detection. *arXiv preprint arXiv:2012.00057*, 2020.
- [19] J. Yang, Z. Ren, M. Xu, X. Chen, D. Crandall, D. Parikh, and D. Batra. Embodied visual recognition. *arXiv preprint arXiv:1904.04404*, 2019.
- [20] M. Lohmann, J. Salvador, A. Kembhavi, and R. Mottaghi. Learning about objects by learning to interact with them. *arXiv preprint arXiv:2006.09306*, 2020.
- [21] J. Wu, I. Yildirim, J. J. Lim, B. Freeman, and J. Tenenbaum. Galileo: Perceiving physical object properties by integrating a physics engine with deep learning. *Advances in neural information processing systems*, 28:127–135, 2015.
- [22] M. Janner, S. Levine, W. T. Freeman, J. B. Tenenbaum, C. Finn, and J. Wu. Reasoning about physical interactions with object-oriented prediction and planning. *arXiv preprint arXiv:1812.10972*, 2018.
- [23] W. Li, S. Azimi, A. Leonardis, and M. Fritz. To fall or not to fall: A visual approach to physical stability prediction. *arXiv preprint arXiv:1604.00066*, 2016.
- [24] I. Lenz, H. Lee, and A. Saxena. Deep learning for detecting robotic grasps. *The International Journal of Robotics Research*, 34(4-5):705–724, 2015.
- [25] J. Redmon and A. Angelova. Real-time grasp detection using convolutional neural networks. In *2015 IEEE International Conference on Robotics and Automation (ICRA)*, pages 1316–1322. IEEE, 2015.
- [26] L. Montesano and M. Lopes. Learning grasping affordances from local visual descriptors. In *2009 IEEE 8th international conference on development and learning*, pages 1–6. IEEE, 2009.
- [27] Y. Qin, R. Chen, H. Zhu, M. Song, J. Xu, and H. Su. S4g: Amodal single-view single-shot se (3) grasp detection in cluttered scenes. In *Conference on robot learning*, pages 53–65. PMLR, 2020.
- [28] M. Kokic, D. Kragic, and J. Bohg. Learning task-oriented grasping from human activity datasets. *IEEE Robotics and Automation Letters*, 5(2):3352–3359, 2020.
- [29] T.-T. Do, A. Nguyen, and I. Reid. Affordancenet: An end-to-end deep learning approach for object affordance detection. In *2018 IEEE international conference on robotics and automation (ICRA)*, pages 5882–5889. IEEE, 2018.
- [30] L. Yang, X. Zhan, K. Li, W. Xu, J. Li, and C. Lu. Cpf: Learning a contact potential field to model the hand-object interaction. *arXiv preprint arXiv:2012.00924*, 2020.
- [31] E. Corona, A. Pumarola, G. Alenya, F. Moreno-Noguer, and G. Rogez. Ganhand: Predicting human grasp affordances in multi-object scenes. In *Proceedings of the IEEE/CVF Conference on Computer Vision and Pattern Recognition*, pages 5031–5041, 2020.
- [32] H. Kjellström, J. Romero, and D. Kragić. Visual object-action recognition: Inferring object affordances from human demonstration. *Computer Vision and Image Understanding*, 115(1): 81–90, 2011.

- [33] K. Fang, T.-L. Wu, D. Yang, S. Savarese, and J. J. Lim. Demo2vec: Reasoning object affordances from online videos. In *Proceedings of the IEEE Conference on Computer Vision and Pattern Recognition*, pages 2139–2147, 2018.
- [34] T. Nagarajan, C. Feichtenhofer, and K. Grauman. Grounded human-object interaction hotspots from video. In *Proceedings of the IEEE/CVF International Conference on Computer Vision*, pages 8688–8697, 2019.
- [35] T. Nagarajan and K. Grauman. Learning affordance landscapes for interaction exploration in 3d environments. In *NeurIPS*, 2020.
- [36] P. Mandikal and K. Grauman. Learning dexterous grasping with object-centric visual affordances. In *IEEE International Conference on Robotics and Automation (ICRA)*, 2021.
- [37] K. Mo, L. Guibas, M. Mukadam, A. Gupta, and S. Tulsiani. Where2act: From pixels to actions for articulated 3d objects. In *International Conference on Computer Vision (ICCV)*, 2021.
- [38] Y. Jiang, M. Lim, C. Zheng, and A. Saxena. Learning to place new objects in a scene. *The International Journal of Robotics Research*, 31(9):1021–1043, 2012.
- [39] M. Tamosiunaite, B. Nemec, A. Ude, and F. Wörgötter. Learning to pour with a robot arm combining goal and shape learning for dynamic movement primitives. *Robotics and Autonomous Systems*, 59(11):910–922, 2011.
- [40] Y. Sun. Ai meets physical world—exploring robot cooking. *arXiv preprint arXiv:1804.07974*, 2018.
- [41] J. A. Haustein, K. Hang, J. Stork, and D. Kragic. Object placement planning and optimization for robot manipulators. *arXiv preprint arXiv:1907.02555*, 2019.
- [42] M. P. Deisenroth, C. E. Rasmussen, and D. Fox. Learning to control a low-cost manipulator using data-efficient reinforcement learning. In *Robotics: Science and Systems VII*, volume 7, pages 57–64, 2011.
- [43] A. H. Quispe, H. B. Amor, and H. I. Christensen. A taxonomy of benchmark tasks for robot manipulation. In *Robotics Research*, pages 405–421. Springer, 2018.
- [44] R. Li, A. Jabri, T. Darrell, and P. Agrawal. Towards practical multi-object manipulation using relational reinforcement learning. In *2020 IEEE International Conference on Robotics and Automation (ICRA)*, pages 4051–4058. IEEE, 2020.
- [45] F. Wang and K. Hauser. Stable bin packing of non-convex 3d objects with a robot manipulator. In *2019 International Conference on Robotics and Automation (ICRA)*, pages 8698–8704. IEEE, 2019.
- [46] J. Stüber, C. Zito, and R. Stolkin. Let’s push things forward: A survey on robot pushing. *Frontiers in Robotics and AI*, 7:8, 2020.
- [47] C. R. Qi, L. Yi, H. Su, and L. J. Guibas. Pointnet++: Deep hierarchical feature learning on point sets in a metric space. In *Advances in neural information processing systems*, pages 5099–5108, 2017.
- [48] A. Zeng, P. Florence, J. Tompson, S. Welker, J. Chien, M. Attarian, T. Armstrong, I. Krasin, D. Duong, V. Sindhwani, et al. Transporter networks: Rearranging the visual world for robotic manipulation. *arXiv preprint arXiv:2010.14406*, 2020.
- [49] C. R. Qi, H. Su, K. Mo, and L. J. Guibas. Pointnet: Deep learning on point sets for 3d classification and segmentation. In *Proceedings of the IEEE conference on computer vision and pattern recognition*, pages 652–660, 2017.
- [50] B. Calli, A. Singh, J. Bruce, A. Walsman, K. Konolige, S. Srinivasa, P. Abbeel, and A. M. Dollar. Yale-cmu-berkeley dataset for robotic manipulation research. *The International Journal of Robotics Research*, 36(3):261–268, 2017.

- [51] G. Research. Threshold ramekin white porcelain. https://fuel.ignitionrobotics.org/1.0/GoogleResearch/models/Threshold_Ramekin_White_Porcelain, 2020.
- [52] G. Research. Room essentials salad plate turquoise. https://fuel.ignitionrobotics.org/1.0/GoogleResearch/models/Room_Essentials_Salad_Plate_Turquoise, 2020.
- [53] G. Research. Us army stash lunch bag. https://fuel.ignitionrobotics.org/1.0/GoogleResearch/models/US_Army_Stash_Lunch_Bag, 2020.
- [54] J. Straub, T. Whelan, L. Ma, Y. Chen, E. Wijmans, S. Green, J. J. Engel, R. Mur-Artal, C. Ren, S. Verma, et al. The replica dataset: A digital replica of indoor spaces. *arXiv preprint arXiv:1906.05797*, 2019.
- [55] R. Martín-Martín, C. Eppner, and O. Brock. The rbo dataset of articulated objects and interactions, 2018.
- [56] G. Research. Threshold porcelain teapot whit. https://fuel.ignitionrobotics.org/1.0/GoogleResearch/models/Threshold_Porcelain_Teapot_White, 2020.

A More Data Details and Visualization

In Table A.3, we summarize our data statistics. In Fig. A.7, we visualize our simulation assets from ShapeNet [6] and PartNet [7] that we use in this work.

There are two kinds of object categories: big heavy objects $\mathcal{C}_{\text{heavy}}$ and small item objects $\mathcal{C}_{\text{item}}$. In our experiments, $\mathcal{C}_{\text{heavy}}$ include cabinets, microwaves, tables, refrigerators, safes, and washing machines, while $\mathcal{C}_{\text{item}}$ contains baskets, bottles, bowls, boxes, cans, pots, mugs, trash cans, buckets, dispensers, jars, and kettles. For the *placement* and *fitting* tasks, we use the object categories in $\mathcal{C}_{\text{heavy}}$ to serve as the main scene object. And, we use the $\mathcal{C}_{\text{item}}$ categories as the scene objects for the other two task environments, as well as employ them as the acting objects for all the four tasks. Some objects may contain articulated parts. For the objects in $\mathcal{C}_{\text{heavy}}$, we sample a random starting part pose that is either fully closed or randomly opened to random degree with equal probabilities. For the acting objects, we fix the part articulation at the rest state during the entire simulated interaction.

B More Details on Settings

For the physical simulation in SAPIEN [5], we use the default setting of frame rate 500 frame-per-second, solver iterations 20, standard gravity 9.81, static friction coefficient 4.0, dynamic friction coefficient 4.0, and restitution coefficient 0.01. The perspective camera is located at a random position determined by a random azimuth $[0^\circ, 360^\circ)$ and a random altitude $[30^\circ, 60^\circ]$, facing towards the center of the scene point cloud with 5 unit length distanced away. It has field-of-view 35° , near plane 0.1, far plane 100, and resolution 448×448 . We use the Three-point lighting with additional ambient lighting. The scene point cloud S samples $n = 10,000$ points using Furthest Point Sampling (FPS) from the back-projected depth scan of the camera.

Train-Cats	All	Basket	Bottle	Bowl	Box	Can	Pot
Train-Data	867	77	16	128	17	65	16
Test-Data	281	43	44	5	18	5	
		Mug	Fridge	Cabinet	Table	Trash	Wash
		134	34	272	70	25	13
		46	9	73	25	10	3
Test-Cats	All	Bucket	Disp	Jar	Kettle	Micro	Safe
Test-Data	637	33	9	528	26	12	29

Table A.3: **Dataset Statistics.** Our experiments use 1,785 ShapeNet [6] models in total, covering 18 commonly seen indoor object categories. We use 12 training categories, which are split into 867 training shapes and 281 test shapes, and 6 test categories with 637 shapes that networks have never seen during training. In the table, disp, micro, wash, and trash are respectively short for dispenser, microwave, washing machine, and trash can.

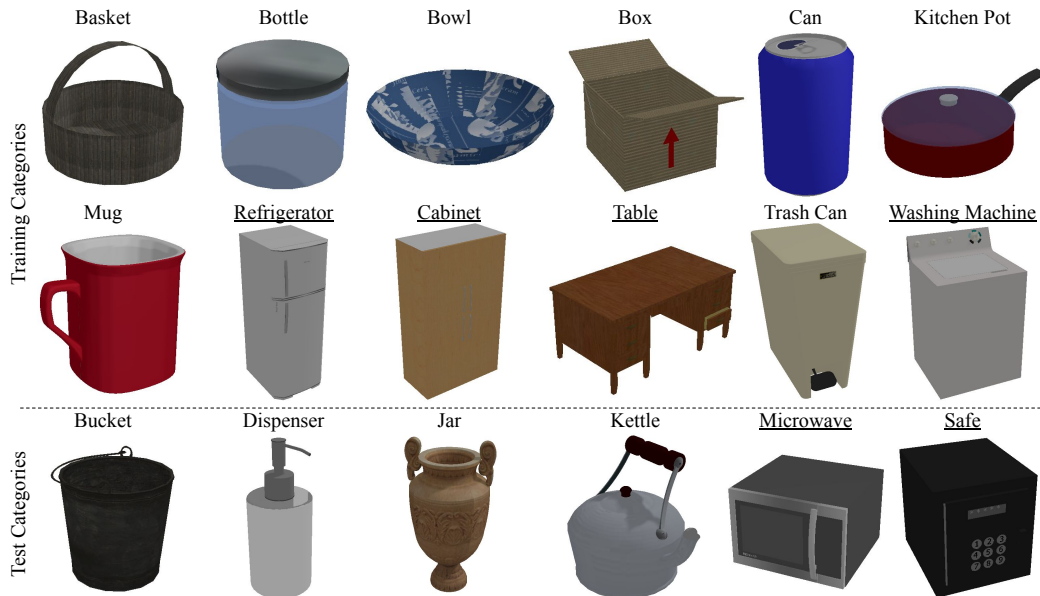


Figure A.7: **Data Visualization.** We visualize one example shape in our simulation assets for each of the 18 object categories we use in this paper. Twelve of them are training object categories while the other six are test categories. We mark with underscore the object categories in $\mathcal{C}_{\text{heavy}}$ that are assumed to be static (heavy).

C More Details on Networks

For the feature extraction backbones $\mathbf{Enc}_{\text{scene}}$ and $\mathbf{Enc}_{\text{object}}$, we use the segmentation-version PointNet++ [47] with a hierarchical encoding stage, which gradually decreases point cloud resolution by several set abstraction layers, and a hierarchical decoding stage, which gradually expands back the resolution until reaching the original point cloud with feature propagation layers. There are skip links between the encoder and decoder. We use the single-scale grouping version of PointNet++. The two PointNet++ networks do not share weights.

More specifically, for $\mathbf{Enc}_{\text{scene}}$, we use four set abstraction layers with resolution 1024, 256, 64 and 16, with learnable Multilayer Perceptrons (MLPs) of sizes [3, 32, 32, 64], [64, 64, 64, 128], [128, 128, 128, 256], and [256, 256, 256, 512] respectively. There are four corresponding feature propagation layers with MLP sizes [131, 128, 128, 128], [320, 256, 128], [384, 256, 256], and [768, 256, 256]. Finally, we use a linear layer that produces a point-wise 128-dim feature map for all scene points. We use ReLU activation functions and Batch-Norm layers.

For $\mathbf{Enc}_{\text{object}}$, we use three set abstraction layers with resolution 512, 128, and 1 (which means that we extract the global feature of the acting object O), with learnable MLPs of sizes [3, 64, 64, 128], [128, 128, 128, 256], and [256, 256, 256, 256] respectively. There are three corresponding feature propagation layers with MLP sizes [131, 128, 128, 128], [384, 256, 256], and [512, 256, 256]. Finally, we use a linear layer that produces a 128-dim feature for every point of the acting object, and use another linear layer to obtain a 128-dim global acting object feature. We use ReLU activation functions and Batch-Norm layers.

We use a PointNet [49] to implement the proposed object-kernel point convolution module $\mathbf{Conv}_{\text{object}}$. The network has three linear layers [256, 128, 128, 128] that transforms each point feature. We use ReLU activation functions and Batch-Norm layers. Finally, we apply a point-wise max-pooling operation to pool over the m acting object points to obtain the aggregated 128-dim feature for every sampled scene seed point p_i .

The final affordance prediction module $\mathbf{Dec}_{\text{critic}}$ is implemented with a simple MLP with two layers [384, 128, 1], with the hidden layer activated by Leaky ReLU and final layer without any activation function. We do not use Batch-Norm for either of the two layers.

D More Details on Training

We collect hundreds of thousands of interaction trials in the simulated task environments for each task. The scene and acting objects are selected randomly from the training data of the training object categories. We equally sample data from different object categories, to address the data imbalance issue. For a generated pair of scene S and acting object O , we then randomly pick an interacting position p_i from the task-specific possible region to perform a simulated interaction. The task environment provides us the final interaction outcome, either successful or failed, using the task-specific metrics described in Sec. 4.2.

Using random data sampling gives us different positive data rate for different tasks, ranging from the lowest one 7.4% for *pushing* and the highest 41.2% for *placement*. We empirically find that having enough positive data samples are essential for a successful training. Thus, for each task, we make sure to sample at least 20,000 successful interaction trials. It is also important to equally sample positive and negative data points in every batch of training.

We use batch size 32 and learning rate 0.001 (decayed by 0.9 every 5000 steps). Each training takes roughly 1-2 days until convergence on a single NVIDIA Titan-XP GPU. The GPU memory cost is about 11 GB. At the test time, the speed is fast (on average 62.5 milliseconds per data) since it only requires a single feed-forwarding inference throughout the network. Testing over a batch of 64 needs 6 GB GPU memory.

E More Results

Fig. E.8 presents more results of our affordance heatmap predictions, to augment Fig. 4 in the main paper.

F More Results on Real-world Data

Fig. F.9 presents more results testing if our learned model can generalize to real-world data, to augment Fig. 5 in the main paper. We use the Replica dataset [54], the RBO dataset [55], and Google Scanned Objects [51, 52, 53, 56] as the input 3D scans.

For qualitative results over the real-world scans shown in Fig. 5 in the main paper, we use an iPad Pro to collect the real-world scans by ourselves. We first mount the camera on a fixed plane and rotate the iPad to make the camera view 20° top down to the ground. We use the front structured light camera on iPad to capture a cluttered table top and a microwave oven.

Our method is designed to learn visual priors for object-object interaction affordance. Future works may further finetune our priors predictions by training on some real-world tasks to obtain more accurate posterior results.

G Failure Cases: Discussion and Visualization

Fig. G.10 summarizes common failure cases of our method. See the caption for detailed explanations and discussions.

We hope that future works may study improving the performance regarding these matters.

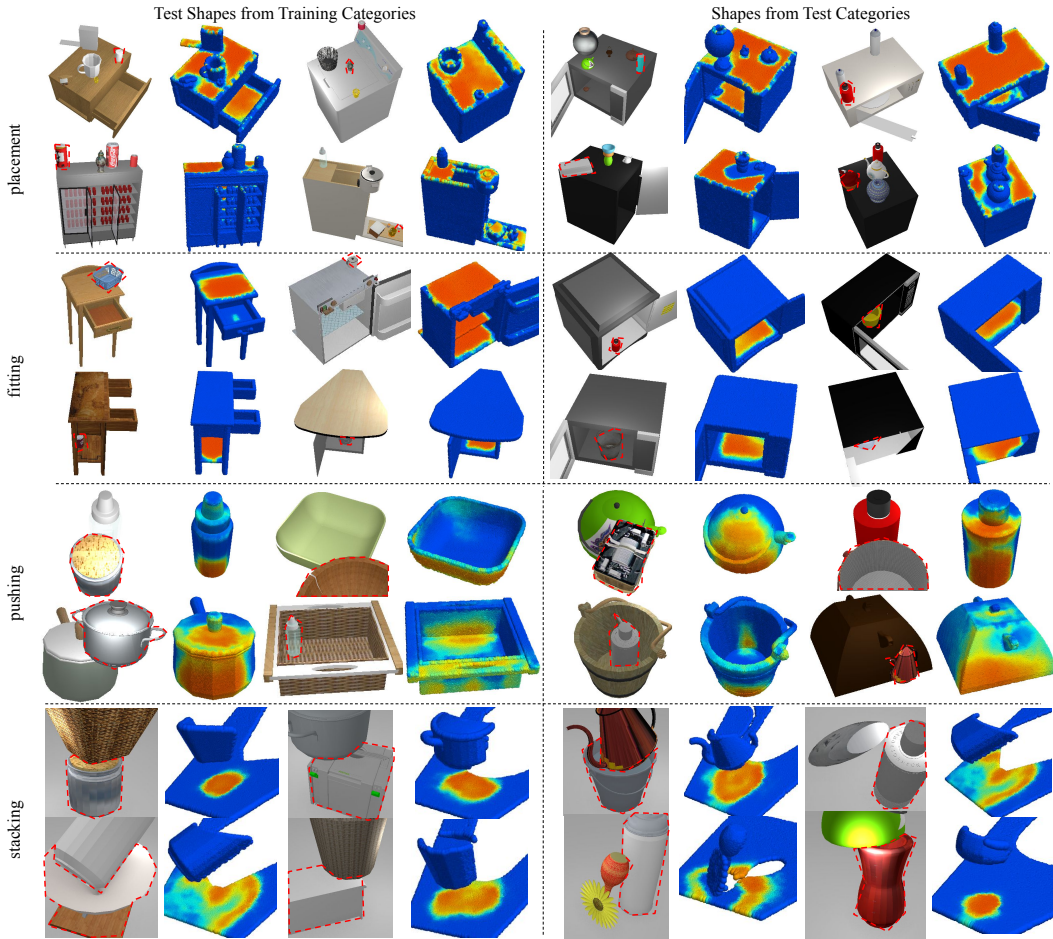


Figure E.8: **More Results.** We present more results of point-wise affordance heatmap predictions, to augment Fig. 4 in the main paper. For each of the tasks, we show examples of our network predictions. Left two examples show test shapes from the training categories, while two right ones are shapes from the test categories. In each pair of result figures, we draw the scene geometry together with the acting object (marked with red dashed boundary) on the left, and show our predicted per-point affordance heatmaps on the right.

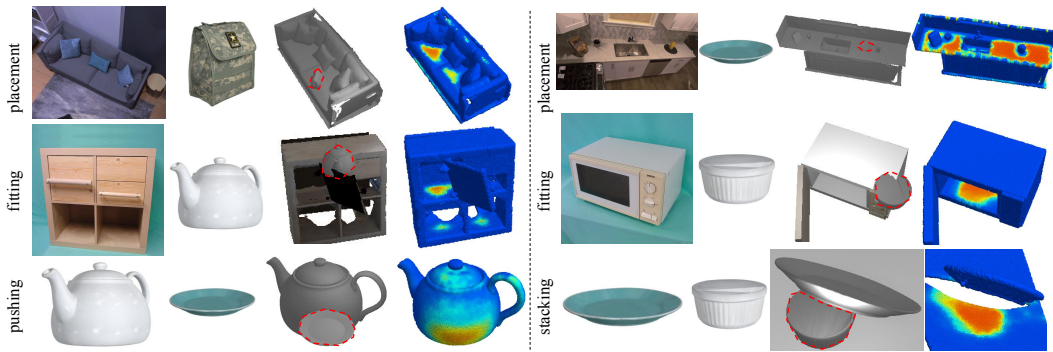


Figure F.9: **More Results on Real-world Data.** From left to right: we respectively show the scene geometry (a partial 3D scan from the camera viewpoint), the acting object (a complete 3D point cloud), the interaction snapshot (to illustrate the poses and sizes of the objects), and our point-wise affordance predictions. For the input 3D scene geometry scans, we use the Replica dataset [54] (the *placement* examples), the RBO dataset [55] (the *fitting* examples), and Google Scanned Objects [52, 56] (the scene geometry for the other two tasks). We use shapes from Google Scanned Objects [51, 52, 53, 56] for the acting objects in the four tasks.

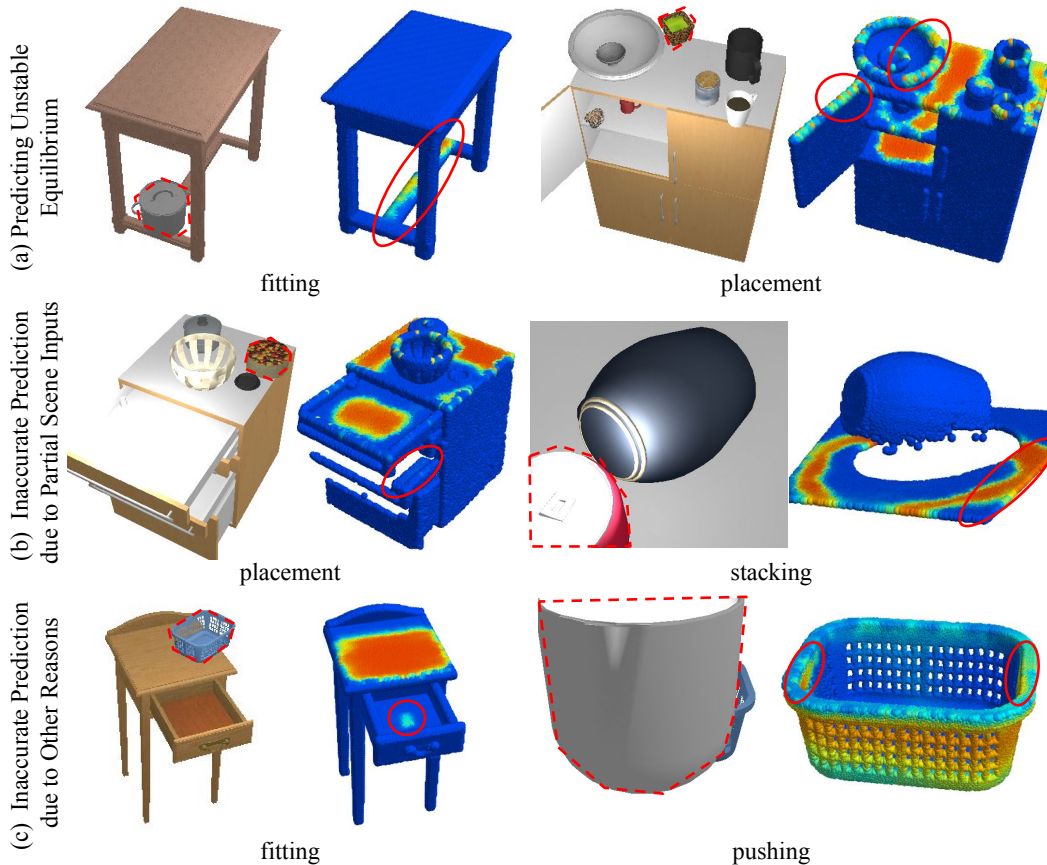


Figure G.10: **Failure Cases.** We visualize common failure cases of our method, by presenting two examples for each of the following categories: predicting unstable equilibrium (a), inaccurate prediction due to partial scene inputs (b), and inaccurate prediction due to other reasons (c). For each pair of results, we show the acting and scene objects on the left, with the acting object marked with red dashed boundary, and our network prediction on the right. On the right image, we explicitly mark out the areas for problematic predictions using red circles. In many real-world scenarios, especially for the *placement* and *fitting* tasks, one might want to find positions for object to be put stably. However, for the examples as shown in (a), we observe some failure cases that unstable equilibrium positions are also predicted, though usually with smaller likelihood scores. For (b), since our network takes as input partial 3D scanned point clouds for the scene geometry, we observe some artifacts in the predictions due to the incompleteness of the input scene point clouds. For instances, one may also put the object in the second drawer, besides the first drawer, in the *placement* example; and in the *stacking* example, one cannot support the jar from the right side. Finally, there are other inaccurate predictions in the examples as shown in (c) due to various reasons: in the *fitting* case, there is an erroneous prediction that the middle of the drawer can fit the basket; and for the *pushing* case, the two side areas should not be pushable. We hope future works can improve upon addressing these issues.